Journal of Membrane Science 731 (2025) 124231

Contents lists available at ScienceDirect

Journal of Membrane Science

journal homepage: www.elsevier.com/locate/memsci

Two-step activation of SSZ-13 zeolite membranes for mild template removal and enhanced CO_2/C_2H_6 separation

Weibo Chen [1], Feng Ye [1], Shuanshi Fan, Yanhong Wang, Xuemei Lang, Gang Li [*]

School of Chemistry and Chemical Engineering, South China University of Technology, Guangzhou, 510641, China

ARTICLE INFO

Keywords:
SSZ-13
Zeolite membrane
Defect
CO_2/C_2H_6 separation
Activation

ABSTRACT

Activation plays a crucial role in determining the final performance of zeolite membranes, and therefore, developing an effective activation technique to achieve both high permeance and high selectivity is highly desirable. In the present study, a promising two-step activation strategy, consisting of a hydrocracking step followed by an oxidation step, has been proposed to fabricate high-performance SSZ-13 zeolite membranes for CO_2/C_2H_6 separation. Compared to the single-step hydrocracking or oxidation activation, the two-step activation strategy enabled much more effective removal of the organic template from the SSZ-13 zeolite channels at a significantly lower temperature, despite identical activation conditions, except for the atmosphere. This led to improved CO_2 permeance and CO_2/C_2H_6 selectivity, owing to the more efficient removal of the template. It was confirmed that C_2H_6 preferentially adsorbs in the SSZ-13 zeolite pores, resulting in reduced CO_2 permeance and CO_2/C_2H_6 selectivity during CO_2/C_2H_6 mixed-gas separation compared to single-gas permeation. Furthermore, the CO_2 permeation mechanism shifted from surface diffusion to activated diffusion due to the narrowing of the zeolite pores after C_2H_6 adsorption. These findings highlight the potential of the proposed two-step activation strategy for developing high-quality zeolite membranes and provide a promising solution for enhancing CO_2/C_2H_6 separation in mixed-gas separations by modifying C_2H_6 adsorption in the zeolite pores.

1. Introduction

C_2H_6 is one of major components of natural gas, and its recovery is highly desirable due to its importance as a petrochemical feedstock for ethylene production [1]. However, CO_2 and C_2H_6 often coexist in natural gas streams, particularly for the associated gas from oil fields obtained using CO_2 enhanced oil recovery (CO_2-EOR) technology. Consequently, the efficient separation of CO_2/C_2H_6 is a critical process in natural gas processing. Conventional processes, such as distillation [2,3] and absorption [4,5], for CO_2/C_2H_6 separation are highly complicated and energy-intensive, which significantly increases operational costs. As a result, there is growing interest in alternative separation technologies that offer more energy-efficient and cost-effective solutions.

Among these alternatives, membrane processes are gaining attention due to their lower energy consumption and simpler operation compared to conventional methods [6–8]. Given the noticeable difference in molecular size between CO_2 (kinetic diameter: 0.33 nm) [9] and C_2H_6 (0.40 nm) [10], zeolite membranes, which have a well-defined pore size at molecular-lever, along with excellent thermal and chemical stability [11–14], present an ideal candidate for efficient CO_2/C_2H_6 separation. Typically, SSZ-13 exhibits a CHA-type zeolite topology with a uniform pore size of 0.38 nm [15], which facilitates the fast diffusion of CO_2 while excluding C_2H_6, making SSZ-13 zeolite membranes a promising choice for CO_2/C_2H_6 separation. Although recent studies have demonstrated that SSZ-13 zeolite membranes can achieve high CO_2 permeance and excellent selectivity against CH_4 [16–20], few studies have specifically focused on the CO_2/C_2H_6 separation.

The activation process of existing zeolite membranes presents several challenges. Typically, activation is achieved by calcining the membrane at high temperatures (≥450 °C) in air or oxygen [21–25], a process that decomposes the occluded organic template within the pores. However, this high-temperature treatment often leads to the formation of grain boundary defects and results in high energy consumption, which negatively impacts both the separation selectivity and the overall economic viability of the membranes [26,27]. To mitigate these issues, one potential solution is to activate the membrane at lower temperatures. Techniques such as ultraviolet radiation [28–30] and ozonation [31–34]

* Corresponding author.
E-mail address: fegli@scut.edu.cn (G. Li).
[1] These authors contributed equally.

https://doi.org/10.1016/j.memsci.2025.124231
Received 10 February 2025; Received in revised form 1 May 2025; Accepted 15 May 2025
Available online 16 May 2025

have been developed for low-temperature activation, although these methods are time-consuming.

Recently, we introduced a hydrocracking activation approach, which allows the decomposition of the organic template at lower temperatures compared to traditional air-based methods [35]. This new technique produced silicalite-1 zeolite membranes with remarkable improved H_2/CO_2 selectivity, resulting from the interaction between CO_2 and the residual template confined in the membrane pores. Despite these improvements, the hydrocracking process only partially removes the template from the zeolite channels, making a relatively poor pore accessibility. As a result, membranes activated using this method exhibited a low H_2 permeance. In the case of CO_2/C_2H_6 separation using SSZ-13 zeolite membranes, it is essential to remove as much of the template as possible for achieving high permeation flux and selectivity.

In this study, we introduce a novel two-step activation method, combining a hydrocracking step followed by an oxidation process, to develop high-performance SSZ-13 zeolite membranes for efficient CO_2/C_2H_6 separation. This two-step activation approach enables more effective removal of the template at relatively lower temperatures, which effectively improves both the selectivity and permeance of the membranes. We believe this activation technique offers a promising pathway to enhance the performance and economic viability of zeolite membranes for practical applications.

2. Experimental

2.1. Materials

An α-Al_2O_3 disc, with an average pore size of 100 nm and a diameter of 25 mm, was used as the support for membrane synthesis. Sodium hydroxide (97%), aluminum hydroxide (99.99%) and N, N, N-trimethyl-1-adamantylammonium hydroxide (TMAdaOH) (25% aqueous solution) were obtained from Shanghai Aladdin Biochemical Technology Co., Ltd. Ethylenediamine (EDA) (99%) was purchased by Guangdong Guangshi Reagent Technology Co., Ltd. Ludox AS-40 colloidal silica (40% in H_2O) was supplied by Sigma-Aldrich.

2.2. Fabrication of SSZ-13 zeolite seeds

SSZ-13 zeolite seeds were prepared according to the following molar composition: 1.0 SiO_2: 0.1 Na_2O: 0.025 Al_2O_3: 0.3 TMAdaOH: 0.3 EDA: 44 H_2O. Briefly, aluminum hydroxide, sodium hydroxide, and water were mixed to achieve a homogeneous solution. TMAdaOH and EDA were then sequentially added, and the mixture was stirred for 3 h. Ludox AS-40 colloidal silica was then slowly added to the solution. After stirring overnight at room temperature, a certain amount of seeds (0.1 wt% of the solution), prepared according to a ball-milling procedure similar to previously reported [36], was added. The resulting mixture was stirred for an additional 1 h to promote a homogeneous dispersion of SSZ-13 seeds within the solution. The final gel solution was then transferred to a polytetrafluoroethylene (PTFE)-lined autoclave and placed in an oven at 160 °C for 96 h. After hydrothermal crystallization, the products were washed and dried at 60 °C overnight to obtain as-synthesized SSZ-13 zeolite powders. Finally, the powders were calcined in air at 650 °C for 6 h with a heating rate of 10 °C min^{-1} to remove the template from the zeolite framework.

2.3. Preparation of SSZ-13 crystals and zeolite membranes

SSZ-13 zeolite seeds were deposited onto the surface of an α-Al_2O_3 support through vacuum-assisted filtration of 1 mL of a 0.2 wt% seed suspension, then dried at 60 °C overnight and calcined at 550 °C for 6 h, resulting in a seeded α-Al_2O_3 support. For membrane growth, a gel precursor, which was prepared using the same synthesis procedure for the SSZ-13 zeolite seeds except the use of modified recipe of SiO_2: Na_2O: Al_2O_3: TMAdaOH: EDA: H_2O = 1.0: 0.1: 0.025: 0.3: 0.1: 44, was used for secondary growth of the seeded α-Al_2O_3 support. The seeded α-Al_2O_3 support was placed into an autoclave and subjected to hydrothermal crystallization at 160 °C for 96 h. After the synthesis, the autoclave was cooled by quenching in running tap water. The resulting as-synthesized SSZ-13 zeolite membrane, along with the SSZ-13 zeolite powders deposited at the bottom of the autoclave, was obtained following washing and drying at 115 °C overnight.

2.4. Activation

SSZ-13 powders and membranes were activated using a two-step process, consisting of a hydrocracking step in a hydrogen atmosphere followed by an oxidation step in an oxygen atmosphere. In the first step, the sample was placed in a quartz tube reactor, and N_2 sweep gas was introduced to remove the air from the reactor. After heating the reactor to the desired temperature for hydrocracking, the nitrogen flow was switched to H_2 at a flow rate of 20 mL min^{-1} to facilitate the decomposition of the template. In the second step, N_2 was used to sweep the reactor and remove H_2 after hydrocracking, followed by the introduction of O_2 at a flow rate of 20 mL min^{-1} to further decompose the template through oxidation.

For comparison, activation of the SSZ-13 zeolite powders and membranes was carried out through a conventional single-step activation process, involving high-temperature calcination in an H_2, O_2, or air atmosphere. The heating and cooling rates during this activation process were both controlled at 1 °C min^{-1}. Zeolite powders activated in hydrogen, oxygen, and air were labeled as PH-*T*-*t*, PO-*T*-*t*, and PA-*T*-*t*, respectively. Likewise, zeolite membranes activated in these gases were referred to MH-*T*-*t*, MO-*T*-*t*, and MA-*T*-*t*, respectively. In these labels, *T* and *t* correspond to the activation temperature and time duration, respectively.

2.5. Characterization

X-ray diffraction (XRD) patterns were collected on a Bruker D8 ADVANCE X-ray diffractometer, operated at 40 kV and 40 mA with Cu-Kα radiation (λ = 0.15418 nm) and a scan speed of 0.2 s $step^{-1}$ over the range of 2θ = 5–60°. Scanning electron microscope (SEM) images were captured using a COXEM EM-30PLUS electron microscope. Thermogravimetric analysis (TGA) and differential scanning calorimetry (DSC) measurements were performed on a NETZSCH STA 449C thermal-gravimetric analyzer, operating from room temperature to 850 °C with a heating rate of 10 °C min^{-1}. Fourier transform infrared (FT-IR) analyses were carried out using a Bruker Tensor FTIR spectrometer. N_2 adsorption-desorption measurements were conducted at 77 K using a Micromeritics ASAP2460 surface area and porosity analyzer. Particle size distribution was determined using a Malvern Mastersizer 3000. Breakthrough curves for a CO_2/C_2H_6 mixture (50/50, v/v) were obtained at 25 °C using a BSD-MAB Multi-component adsorption breakthrough curve analyzer. CO_2 and C_2H_6 adsorption-desorption tests were conducted at 30 and 50 °C using a Quantachrome Autosorb-iQ-2 automated surface area and pore size analyzer.

2.6. Membrane permeation testing

The SSZ-13 zeolite membrane was mounted in a custom-built module using an O-ring to prevent any leaks. The membrane module was then placed in a tubular furnace for permeation measurements, with the temperature maintained between 25 and 200 °C. The feed pressure was controlled in the range of 0.2–0.5 MPa. The permeate pressure was kept at 0.1 MPa. Membrane permeation tests were conducted using single gases (He, H_2, CO_2, N_2, CH_4, C_2H_6, C_3H_8, and i-C_4H_{10}) and an equimolar CO_2/C_2H_6 binary mixture. The gas flow rate was determined using a bubble flow meter, while the gas composition was analyzed using a FULI 9790II gas chromatograph (GC) equipped with a thermal conductivity detector (TCD). Further information on the experimental apparatus for

the membrane permeation measurement is detailed in our previous work [35].

The gas permeance of component i was calculated according to Eq. (1), as follows:

$$P_i = \frac{J_i}{A \cdot \Delta p_i} \tag{1}$$

where P_i and J_i are the permeance and molar flow rate through the membrane for component i; A is the membrane permeation area; and Δp_i is the partial pressure difference across the membrane for component i between the feed side and the permeate side. The ideal selectivity ($\alpha_{i/j}^{ideal}$) and separation selectivity ($\alpha_{i/j}^{sep}$) were defined as the permeance ratio of component i to j in the single-component and multi-component gas systems, as described in Eqs. (2) and (3), respectively.

$$\alpha_{i/j}^{ideal} = \frac{P_i}{P_j} \tag{2}$$

$$\alpha_{i/j}^{sep} = \frac{P_i}{P_j} \tag{3}$$

3. Results and discussion

3.1. SSZ-13 zeolite powder activation through single-step and two-step processes

Fig. 1a shows the XRD pattern of the as-synthesized zeolite powders collected from the bottom of the autoclave after membrane growth. The characteristic peaks of the sample matched those of SSZ-13 zeolite (PDF#47–0762) very well, which confirms the collected powders were well crystallized SSZ-13 zeolites. The SEM image of the as-synthesized SSZ-13 zeolite powders, presented in Fig. 1b, showed cubic morphologies with particle sizes between 1 and 3 μm. These powders were employed for activation studies under various conditions.

Fig. 2a shows the XRD patterns of SSZ-13 zeolite powders activated in single-step and two-step processes under various activation conditions. All samples showed characteristic peaks matching with the CHA-type zeolite, regardless of the calcination temperature, duration, and atmosphere, which indicates that all SSZ-13 zeolites maintained their crystallographic structure during the activation process because of their excellent thermal stability.

Fig. 2b shows the FT-IR spectra of the SSZ-13 zeolite powders activated using both single-step and two-step processes under various activation conditions. The peaks observed at 538 and 642 cm^{-1} are linked to the bending vibrations of the D6R, while the peaks at 460 cm^{-1} corresponds to the symmetric stretching vibration of T−O bonds (Si–O or Al–O) [37]. The band at 670 cm^{-1} is associated with the symmetric stretching of T−O−T within the *cha* cage structure [38]. Peaks at 790 and 1060 cm^{-1} are attributed to the asymmetric stretching of Al–O and the asymmetric bending of O−T−O bonds [39], respectively. The above bands, related to the framework vibrations of the SSZ-13 zeolite crystalline structure, were consistently present across all samples, regardless of the activation method, indicating that the framework of zeolites remained intact during activation. Additionally, the bands around 3460 cm^{-1} and 1630 cm^{-1} observed in all spectra are assigned to the Si–OH stretching and the H–O–H stretching of adsorbed water [40,41], respectively. Of particular note, the intensity of the bands at 1300, 1415, 1485, 2870, 2928, and 2960 cm^{-1}, which are associated with the template present in the zeolite [42,43], was significantly reduced in samples treated at 350 °C using single-step and two-step processes (PH-350-30, PO-350-30, PH-350-20@PO-350-10, PH-350-10@PO-350-20). This suggests that the template underwent partial decomposition at 350 °C. In contrast, these bands completely absent in PA-500-6, which underwent calcination at a high temperature of 500 °C.

Fig. 2c presents the TGA curves of SSZ-13 zeolite powders activated using single-step and two-step processes under various activation conditions, and the corresponding DSC curves are shown in Fig. S1. The as-synthesized SSZ-13 zeolite exhibited a significant mass loss of approximately 21% in the temperature range of 400–700 °C, which corresponds to the degradation of the template within the zeolite channels. When the SSZ-13 zeolite was hydrocracked at 350 °C for 30 h, the weight loss was slightly lower than that of the as-synthesized SSZ-13 zeolite, suggesting that the template may have undergone some structural changes in its chemical structure but was not effectively removed after the hydrocracking treatment. However, when the SSZ-13 zeolite was oxidized in oxygen at 350 °C for 30 h, the weight loss decreased to approximately 19%, indicating that the oxygen atmosphere was more effective than the hydrogen atmosphere in removing the template at 350 °C. Interestingly, when the activation process was divided into two steps, first hydrocracking and then oxidation, the weight loss was significantly lower than that observed for the sample activated with either a single hydrocracking or oxidation step for the same duration. For instance, the sample activated with 10 h of hydrocracking and 20 h of oxidation exhibited a remarkable reduction in weight loss, reaching approximately 9%. Moreover, DSC curves also showed a smaller exotherm effect for the zeolite activated via the two-step process, further confirming that this activation technique removed more template from the SSZ-13 zeolite. In contrast, the conventional single oxidation activation required a temperature approximately 500 °C to remove the considerable weight of the template, which is 150 °C higher than the temperature required for the two-step activation process. These results suggest that the hydrocracking step has a significant impact on the subsequent oxidation step, facilitating the removal of most of the template during the oxidation process at much lower temperatures.

As further confirmed by N_2 adsorption-desorption isotherms in Fig. 2d and pore structural parameters in Table 1, SSZ-13 zeolite

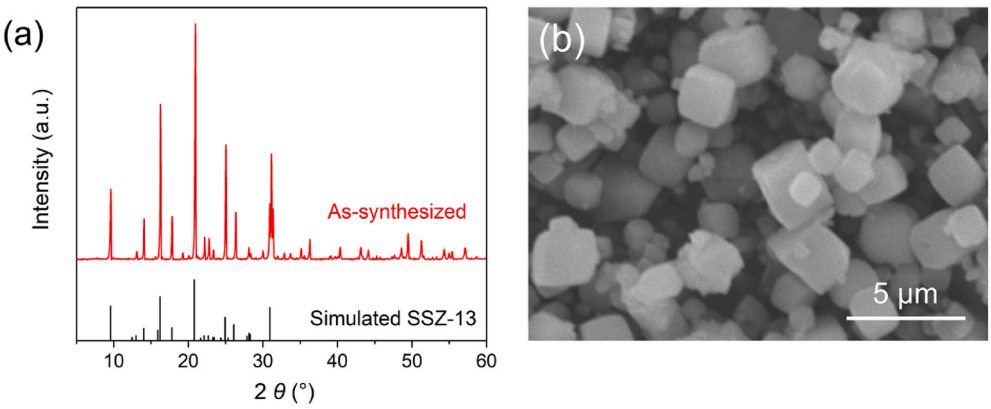

Fig. 1. (a) XRD pattern and (b) SEM image of the as-synthesized SSZ-13 zeolite powders.

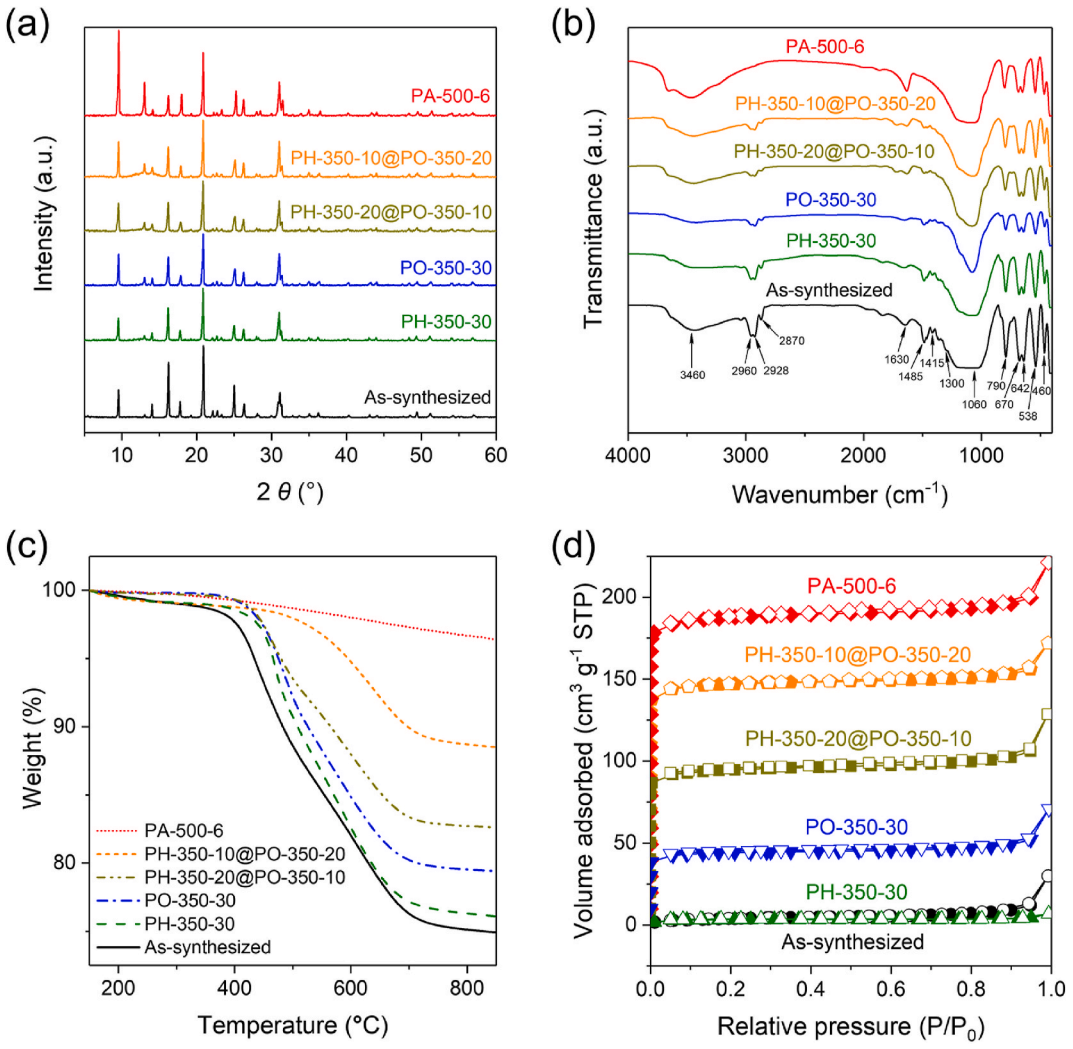

Fig. 2. (a) XRD patterns, (b) TGA curves, (c) FT-IR spectra, and (d) N_2 adsorption-desorption isotherms (Closed symbols: adsorption; Open symbols: desorption) of the SSZ-13 zeolites in their as-synthesized state and after single-step and two-step activation treatments.

Table 1
Pore structural parameters of SSZ-13 zeolites.

Sample	S_{BET} (m^2 g^{-1})	V_{pore} (cm^3 g^{-1})	V_{micro} (cm^3 g^{-1})	V_{meso} (cm^3 g^{-1})
As-synthesized	13.58	0.044	0.000	0.044
PH-350-30	10.68	0.009	0.003	0.006
PO-350-30	131.77	0.105	0.061	0.044
PH-350-20@PO-350-10	288.36	0.191	0.133	0.058
PH-350-10@PO-350-20	445.65	0.260	0.215	0.045
PA-500-6	569.47	0.332	0.272	0.060

activated through a single hydrocracking step at 350 °C for 30 h exhibited an extremely low BET surface area (10.68 m^2 g^{-1}) and micropore volume (0.003 cm^3 g^{-1}), which were almost identical to those measured for the as-synthesized SSZ-13 zeolite, in agreement with the results obtained from the TGA curves (Fig. 2c). Since the template could be partially removed during the single oxidation step, the SSZ-13 zeolite calcined at 350 °C for 30 h in oxygen showed both increased BET surface area (288.36 m^2 g^{-1}) and micropore volume (0.133 cm^3 g^{-1}). However, these values were still much lower than those measured for the SSZ-13 zeolite calcined at 500 °C for 6 h in air (569.47 m^2 g^{-1} and 0.272 cm^3 g^{-1}), confirming that a significant amount of template remained in the zeolite channels. In contrast, the two-step activation process significantly increased both the BET surface area and micropore volume. For instance, the SSZ-13 zeolite activated with 10 h of hydrocracking followed by 20 h of oxidation at 350 °C exhibited a BET surface area and a micropore volume as high as 445.65 m^2 g^{-1} and 0.215 cm^3 g^{-1}, which were quite close to those measured for the sample calcined at 500 °C for 6 h in air. This observation further confirms that the proposed two-step activation strategy effectively removes the template from zeolite channels at a much lower temperature.

The FT-IR, TGA, and N_2 adsorption-desorption results collectively led to a conclusion that the hydrocracking step only partially decomposed the template in the SSZ-13 zeolite, resulting in slight pore opening and potential changes in the template structure, which enhanced template removal during the subsequent oxidation step. Lang et al. [44] previously reported that the first hydrocracking step is crucial for the low-temperature removal of template from MFI zeolite. Coke-like residues, which typically form during low-temperature activation in air and are difficult to remove [45,46], were not observed during the subsequent low-temperature oxidation process. They attributed this phenomenon to a special propyl-radical mechanism for template degradation in the H_2 atmosphere, and the small template residue could then be more easily removed by the following oxidation step due to improved gas diffusion after hydrocracking. Therefore, the high efficiency of the two-step activation process for SSZ-13 zeolite in the present

study, compared to the traditional single-step activation technique, is likely due to the prevention of stable coke-like residue formation and enhanced gas diffusion within the zeolite. This novel two-step activation technique makes it an attractive approach for the low-temperature activation of zeolite membranes with significantly reduced grain boundary defects and lower manufacturing costs.

3.2. SSZ-13 zeolite membrane activation through single-step and two-step processes

Fig. 3a shows the XRD pattern of the as-synthesized SSZ-13 zeolite seeds. The characteristic peaks were in good agreement with those of the CHA-type zeolite, thereby validating the successful synthesis of SSZ-13 zeolite seeds. The DLS particle size distribution (Fig. 3b) and SEM image (inset in Fig. 3b) further indicated that the SSZ-13 zeolite seeds exhibited a uniform particle size of approximately 400 nm, which was somewhat above the mean pore size of the α-Al_2O_3 disc. As a result, the particles were well-suited for forming a highly uniform and compact seed layer via vacuum filtration. This high-quality seeded support was crucial for the secondary growth of compact SSZ-13 zeolite membranes.

Fig. 4a and b shows SEM images of the surface and cross-section of the seeded α-Al_2O_3 support. SSZ-13 zeolite seeds were uniformly deposited onto the surface of the α-Al_2O_3 support, forming a continuous SSZ-13 seed layer approximately 2 μm in thickness. Fig. 4c and d shows top-view and cross-sectional SEM images of the SSZ-13 zeolite membrane. The membrane was composed of well-intergrown SSZ-13 zeolite crystals, with a thickness of around 3 μm. It was free from visible cracks and pinholes, and impermeable to He before activation, confirming the successful formation of a high-quality zeolite membrane after the secondary growth process.

Table 2 shows the He and C_3H_8 single-gas permeation performance of SSZ-13 zeolite membranes prepared using both single-step and two-step activation processes under various calcination temperatures and durations. In the single-step hydrocracking activation at 300 and 350 °C, the SSZ-13 zeolite membrane exhibited low He permeance, on the orders of magnitude ranging from 10^{-10} to 10^{-9} mol Pa^{-1} m^{-2} s^{-1}, while C_3H_8 was nearly impermeable. This indicates that the template was not effectively degraded within the zeolite channels, even when the hydrocracking duration was extended from 10 to 30 h. This observation aligns with the TGA results shown in Fig. 2c. When the hydrocracking temperature was increased to 400 °C, the membrane permeance improved approximately by one order of magnitude, but the He/C_3H_8 ideal selectivity was only 27, suggesting the generation of considerable grain boundary defects in the SSZ-13 zeolite membrane at a high temperature. Therefore, the hydrocracking temperature should be controlled at approximately 350 °C.

It should be noted that in the two-step process, consisting of hydrocracking activation followed by oxidation activation, both at 350 °C, the He permeance of the resulting SSZ-13 zeolite membrane reached an order of magnitude of 10^{-7} mol Pa^{-1} m^{-2} s^{-1}, with a superior He/C_3H_8 ideal selectivity ranging from 300 to 400. This He permeance was comparable to, or even higher than, that reported in the literature [16, 47–49], where the membrane activation was performed through a single-step oxidation process at higher temperatures (450–550 °C). For further comparison, we also conducted membrane activation using a single-step oxidation process in air and O_2, respectively, at 350 °C for 30 h. However, the membranes showed lower He permeances and He/C_3H_8 ideal selectivities. When the membrane activation was carried out at a higher temperature of 500 °C in air, although it demonstrated a high He permeance of 5.1×10^{-7} mol Pa^{-1} m^{-2} s^{-1} after just 6 h of calcination, it lacked sufficient selectivity in gas separation, implying that significant defects had generated in the membrane because of the high calcination temperature. The above results suggest that the two-step activation process, consisting of hydrocracking followed by oxidation at a relatively low temperature, was more favorable for fabricating zeolite membranes with high flux and high selectivity. This can be attributed to the pre-degradation of the template by hydrocracking, which facilitates its removal through the subsequent oxidation process at low temperatures. To further investigate the reproducibility of the membranes, an additional eight SSZ-13 zeolite membranes were prepared under the same conditions as those used for the MH-350-10@MO-350-20 membrane (Table S1). A comparable performance to that of the MH-350-10@MO-350-20 membrane was observed in these membranes, demonstrating that the two-step activation method is highly reproducible and effective in fabricating high-performance SSZ-13 zeolite membranes.

3.3. Single-gas permeation performance

Fig. 5a presents the single-gas permeance of the SSZ-13 zeolite membrane (MH-350-10@MO-350-20), fabricated via a two-step activation process, as a function of kinetic diameter under 25 °C. For comparison, the single-gas permeance of another membrane (MA-500-6), prepared through a conventional single-step activation process, is also shown in Fig. 5a. The MH-350-10@MO-350-20 membrane exhibited H_2 and CO_2 permeances of 1.6×10^{-7} and 2.0×10^{-7} mol Pa^{-1} m^{-2} s^{-1}, with H_2/C_2H_6, H_2/C_3H_8, H_2/i-C_4H_{10}, and CO_2/C_2H_6 ideal selectivities of 170, 376, 675 and 211 (Fig. 5b) at 25 °C. In contrast, the MA-500-6 membrane showed much higher H_2 and CO_2 permeances of 5.7×10^{-7} and 6.4×10^{-7} mol Pa^{-1} m^{-2} s^{-1}, but much lower H_2/C_2H_6, H_2/C_3H_8, H_2/i-C_4H_{10}, and CO_2/C_2H_6 ideal selectivities, which were close to Knudsen selectivity values (Fig. 5b). Moreover, the MH-350-10@MO-350-20 membrane exhibited extremely stable gas permeation performance at 25 °C (Fig. 6). This result further confirms that the low-temperature two-step activation process proposed in this work is more advantageous than the conventional single-step activation process for

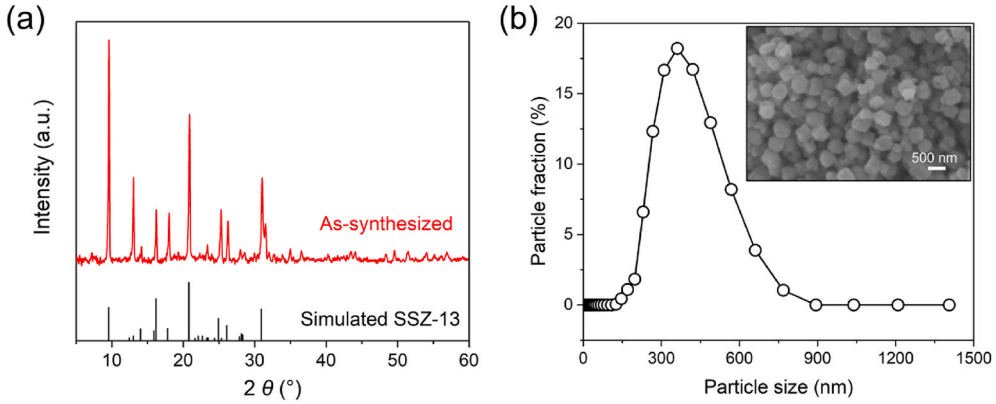

Fig. 3. (a) XRD pattern and (b) DLS particle size distribution of the as-synthesized SSZ-13 zeolite seeds. Inset in Fig. 3b is SEM image of the SSZ-13 zeolite seeds.

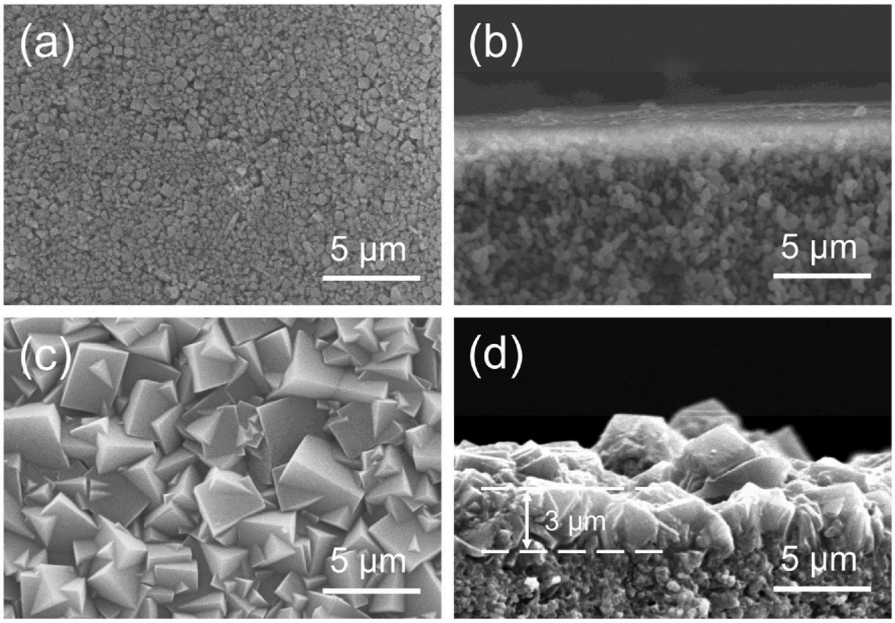

Fig. 4. Top-view and cross-sectional SEM images of (a, b) the SSZ-13 seed layer and (c, d) the SSZ-13 zeolite membrane.

Table 2
Permeation performance of SSZ-13 zeolite membranes activated under various conditions.

Membrane	He permeance (mol Pa^{-1} m^{-2} s^{-1})	C_3H_8 permeance (mol Pa^{-1} m^{-2} s^{-1})	He/C_3H_8 ideal selectivity (–)
MH-300-10	8.4×10^{-10}	$<10^{-12}$	>840
MH-300-20	8.7×10^{-10}	$<10^{-12}$	>870
MH-350-10	1.1×10^{-9}	$<10^{-12}$	>1100
MH-350-20	3.3×10^{-9}	$<10^{-12}$	>3300
MH-350-30	3.4×10^{-9}	$<10^{-12}$	>3400
MH-400-20	5.1×10^{-8}	1.9×10^{-9}	27
MA-350-30	2.2×10^{-9}	1.0×10^{-10}	22
MO-350-30	4.6×10^{-8}	2.6×10^{-10}	177
MH-350-20@MO-350-10	9.6×10^{-8}	2.8×10^{-10}	343
MH-350-10@MO-350-20	1.3×10^{-7}	4.3×10^{-10}	302
MA-500-6	5.1×10^{-7}	2.4×10^{-7}	2

producing high-performance SSZ-13 zeolite membranes, due to the more effective removal of the template at lower temperatures, as confirmed by TGA results in Fig. 2c. Compared with most previously reported zeolite membranes for CO_2/C_2H_6 separation (Table S2), the SSZ-13 zeolite membranes prepared in this work exhibit an enhanced performance, demonstrating the promise of the two-step activation strategy for high-performance zeolite membrane fabrication.

Fig. 7 illustrates the single-component permeance through the two-step activated MH-350-10@MO-350-20 membrane as a function of temperature. The permeances of He, H_2, CH_4, C_2H_6, C_3H_8, and i-C_4H_{10} enhanced with temperature, suggesting that their permeation is governed by an activated diffusion mechanism, owing to the small size difference between the gas molecules and their permeation channels. In contrast, the permeances of CO_2 and N_2 decreased as the temperature increased, indicating that surface diffusion governs CO_2 and N_2 permeation through the zeolite channels, driven by strong adsorption effects [9,50]. Although hydrocarbons can also be strongly adsorbed on SSZ-13 zeolite, the distinct permeation mechanism can be attributed primarily to the different permeation channels within the membrane.

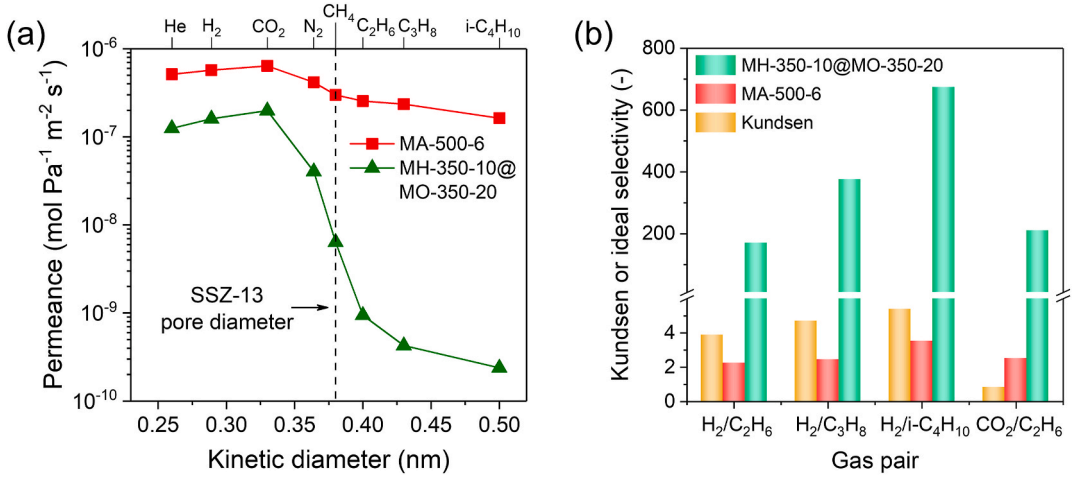

Fig. 5. (a) Single-gas permeances through SSZ-13 zeolite membranes for gases with different kinetic diameters under 25 °C. (b) Selectivities of SSZ-13 zeolite membranes for separating various gas pairs.

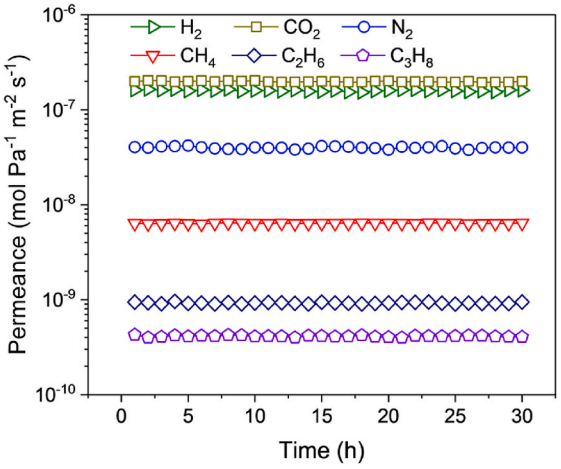

Fig. 6. Time-dependent singe-gas permeance at 25 °C for the two-step activated MH-350-10@MO-350-20 membrane.

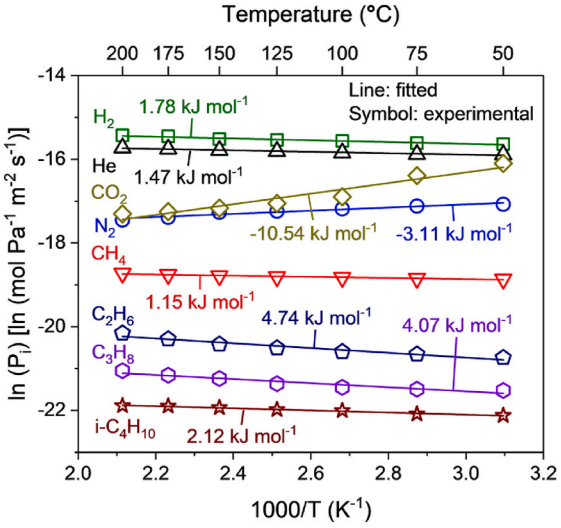

Fig. 7. Single-component permeances through the two-step activated MH-350-10@MO-350-20 membrane as a function of temperature.

The molecular sizes of hydrocarbons are close to or larger than the SSZ-13 zeolite pores (0.38 nm), implying that these hydrocarbons most likely permeate through membrane defects. The high ideal selectivity of He over hydrocarbons suggests that the membrane defects are relatively small, which leads to an activated diffusion for hydrocarbon transport. This observation further confirms the successful fabrication of high-quality SSZ-13 zeolite membranes via the two-step activation process.

The gas permeation activation energy can be determined by fitting the gas permeance to temperature using the Arrhenius equation, as shown in Eq. (4):

$$P_i = k_i \cdot exp\left(-\frac{E_i}{RT}\right) \quad (4)$$

where k_i is the pre-exponential factor for component i, E_i is the activation energy for gas permeation through the membrane, R is the ideal gas constant, and T is the permeation temperature.

The activation energies for He and H_2 transport through the MH-350-10@MO-350-20 membrane, which was prepared via a two-step hydrocracking-oxidation activation process, were calculated as 1.47 and 1.78 kJ mol^{-1}, respectively. These values were significantly smaller than those of the membrane activated via the single-step hydrocracking process (He: 7.10 kJ mol^{-1}; H_2: 8.98 kJ mol^{-1}) [51]. This suggests that the two-step activation process led to a larger average pore size, likely due to further oxidation of the residual template following hydrocracking activation, which gradually enlarged the membrane pores. On the other hand, the activation energies for hydrocarbons, such as CH_4 and C_2H_6, which are expected to primarily permeate through the grain boundary defects, were 1.15 and 4.74 kJ mol^{-1}, respectively. These values were much lower and comparable to those of the SSZ-13 zeolite membrane prepared via the single-step hydrocracking activation (CH_4: 5.71 kJ mol^{-1}; C_2H_6: 4.77 kJ mol^{-1}) [51], further supporting the formation of a relatively looser pore structure with reasonably controlled grain boundary defects. Therefore, compared to the membrane fabricated via the single-step hydrocracking activation process, the MH-350-10@MO-350-20 membrane, prepared via the two-step hydrocracking-oxidation activation process, demonstrated a higher permeance and a greater CO_2/C_2H_6 ideal selectivity. These results suggest that the two-step hydrocracking-oxidation activation process holds promise for developing high-performance CO_2/C_2H_6 separation SSZ-13 zeolite membranes.

3.4. Separation of the binary CO_2/C_2H_6 mixture

Fig. 8a shows the permeation performance of the two-step activated MH-350-10@MO-350-20 membrane for separating an equimolar CO_2/C_2H_6 mixture as a function of feed pressure at 25 °C. Both CO_2 and C_2H_6 decreased as the feed pressure increased, this is because the chemical potential gradient of the adsorbed CO_2 and C_2H_6 decreased as the coverage approaches saturation at a higher feed pressure [50,52]. Furthermore, compared with CO_2/C_2H_6 ideal selectivity of 211 for the single-gas permeation at the same feed pressure at 0.2 MPa, the CO_2/C_2H_6 selectivity of 19 for separating an equimolar CO_2/C_2H_6 mixture was much lower, mainly due to a much lower CO_2 permeance in the CO_2/C_2H_6 mixture system. A similar reduction in CO_2 permeance was reported by Chisholm et al. [53], who observed this effect upon introducing 15% C_2H_6 into the CO_2 feed. In another study. Wu et al. [54] also found that the H_2 permeance decreased by 54.2% and 62.5% when 1 mol% and 5 mol% C_2H_6 were added to an $H_2/CH_4/C_2H_6$ ternary mixture, respectively. More recently, Gong et al. [55] reported 14% and 11% reductions in He and CH_4 permeances, respectively, after a one-day permeation test, even when only 1 mol% C_2H_6 was present in the $He/N_2/CH_4$ ternary feed. It was suggested that these phenomena resulted from the strong adsorption of C_2H_6 in the zeolite pores [53–55]. To further confirm the cause of those phenomena, we measured both CO_2 and C_2H_6 adsorption-desorption isotherms at 30 and 50 °C, respectively, as shown in Fig. 9. Both CO_2 and C_2H_6 could be effectively adsorbed in the SSZ-13 zeolite pores, although the kinetic diameter (0.40 nm) was reported [10] slightly exceeding the pore opening of the SSZ-13 zeolite (0.38 nm). This C_2H_6 adsorption behavior was similar to that observed in pure silica CHA zeolite in a previous study [54]. The calculated adsorption heats for C_2H_6 were higher than those for CO_2, particularly at higher adsorption amounts. This indicates a stronger interaction of C_2H_6 with the SSZ-13 zeolite membrane compared to CO_2, potentially explaining its preferential adsorption. The breakthrough curves of the SSZ-13 zeolite for a CO_2/C_2H_6 mixture (50/50, v/v) (Fig. 10) further suggest that C_2H_6 was preferentially adsorbed in the SSZ-13 zeolite pores. The above observation confirms that the decreased CO_2 permeance and CO_2/C_2H_6 selectivity for the MH-350-10@MO-350-20 membrane was ascribed to the competitive adsorption of C_2H_6 on the membrane in the CO_2/C_2H_6 binary mixture.

Fig. 8b shows the permeation performance of the two-step activated MH-350-10@MO-350-20 membrane for separating an equimolar CO_2/C_2H_6 mixture as a function of temperature at feed pressure of 0.2 MPa. Similar to the temperature dependence observed for C_2H_6 during single-gas permeation, the C_2H_6 permeance increased with temperature. However, the CO_2 permeance exhibited a different trend, increasing

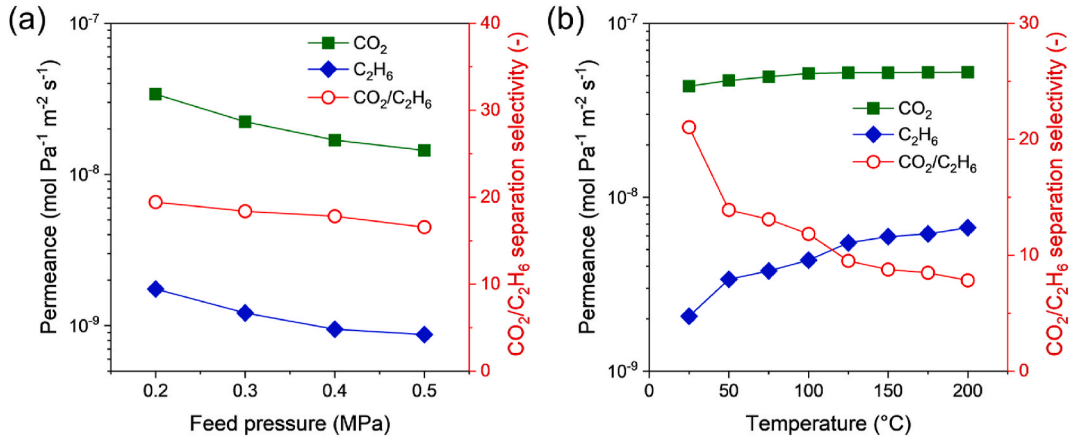

Fig. 8. Permeation performance of the two-step activated MH-350-10@MO-350-20 membrane for separating an equimolar CO_2/C_2H_6 mixture as a function of (a) feed pressure, and (b) temperature.

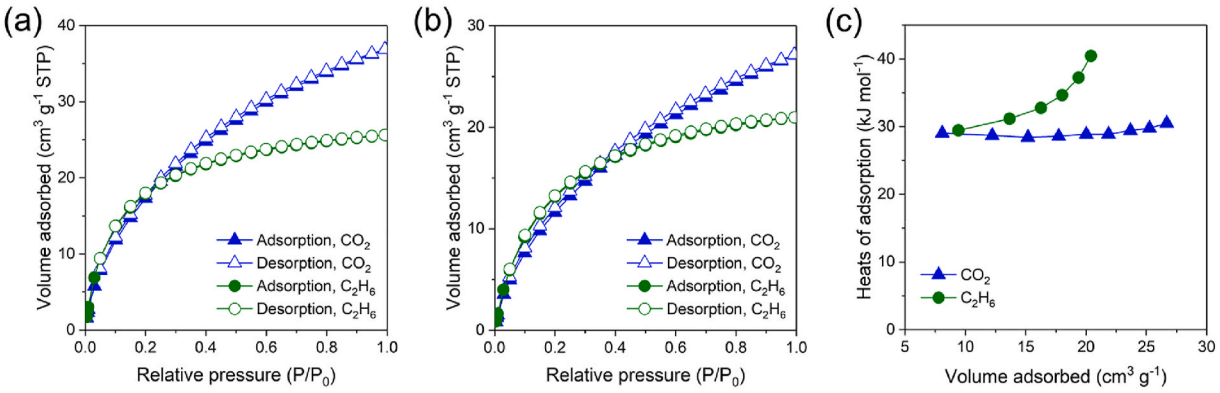

Fig. 9. CO_2 and C_2H_6 adsorption-desorption isotherms of SSZ-13 crystals measured at (a) 30 and (b) 50 °C. (c) Heats of CO_2 and C_2H_6 adsorption on SSZ-13 crystals as a function of volume adsorbed.

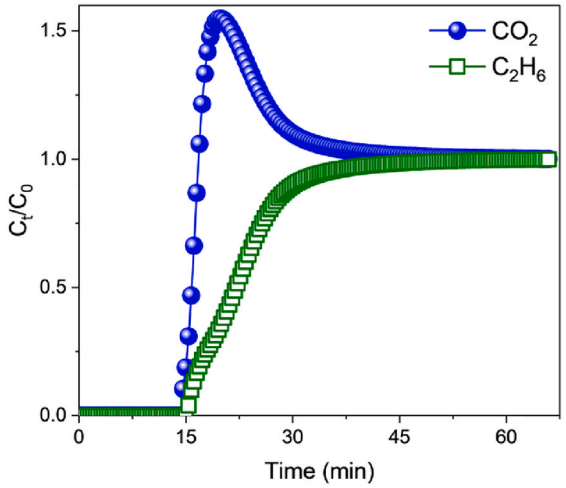

Fig. 10. Breakthrough curves of SSZ-13 zeolites for a CO_2/C_2H_6 (50/50, v/v) mixture measured at 25 °C.

with temperature, which contrasts with the behavior observed during single-gas permeation. As a result, the CO_2/C_2H_6 selectivity decreased only slightly when the temperature was increased from 25 to 200 °C. This result suggests that the CO_2 transport mechanism shifted from the surface diffusion in the single-gas system to the activated diffusion in the CO_2/C_2H_6 binary mixture system. This shift is most likely due to the narrowing of the membrane pore size after the adsorption of C_2H_6 molecules. The difference in CO_2 transport mechanisms between single-gas and CO_2/C_2H_6 mixed-gas permeation further supports the preferential adsorption of C_2H_6 over CO_2 in the SSZ-13 zeolite membrane.

Fig. 11 shows the stability of the two-step activated MH-350-10@MO-350-20 membrane for separating an equimolar CO_2/C_2H_6 mixture at 25 °C and feed pressure of 0.2 MPa. The CO_2 and C_2H_6 permeances were about 4.0×10^{-8} and 2.0×10^{-9} mol Pa^{-1} m^{-2} s^{-1},

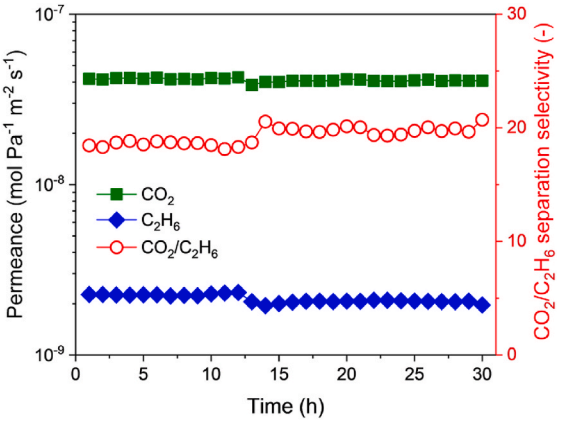

Fig. 11. Time-dependent gas permeance through the two-step activated MH-350-10@MO-350-20 membrane for separating an equimolar CO_2/C_2H_6 mixture at 25 °C.

respectively, and remained almost constant over 30 h testing period, with a CO_2/C_2H_6 selectivity of approximately 20. These results demonstrate the excellent stability of the membrane for CO_2/C_2H_6 separation, suggesting the potential of SSZ-13 zeolite membranes for practical applications in CO_2/C_2H_6 separation processes.

4. Conclusions

A two-step activation technique, consisting of a hydrocracking step followed by an oxidation process, has been proposed to develop high-quality SSZ-13 zeolite membranes for CO_2/C_2H_6 separation. The first hydrocracking step effectively facilitates the easier removal of the organic template from the zeolite channels during the subsequent oxidation step, enabling at a much lower temperature than either single hydrocracking or oxidation activation. As a result, the resultant membrane exhibits improved gas permeance and selectivity, attributed to the formation of fewer grain boundary defects and enhanced template removal. During single-gas permeation, CO_2 transport through the membrane follows the surface diffusion mechanism, while during CO_2/C_2H_6 mixed-gas permeation, it follows the activated diffusion mechanism. This mechanism shift can be attributed to the preferential adsorption of C_2H_6 over CO_2 in the SSZ-13 zeolite pores.

CRediT authorship contribution statement

Weibo Chen: Writing – original draft, Investigation, Formal analysis, Data curation. **Feng Ye:** Writing – original draft, Investigation. **Shuanshi Fan:** Writing – review & editing, Methodology. **Yanhong Wang:** Writing – review & editing. **Xuemei Lang:** Writing – review & editing, Project administration. **Gang Li:** Writing – review & editing, Supervision, Funding acquisition, Conceptualization.

Declaration of competing interest

The authors declare that they have no known competing financial interests or personal relationships that could have appeared to influence the work reported in this paper.

Acknowledgments

This research was financially supported by the Fundamental Research Funds for the Central Universities (grant number 2024ZYGXZR100) and the Guangdong Basic and Applied Basic Research Foundation (grant number 2022A1515012066).

Appendix A. Supplementary data

Supplementary data to this article can be found online at https://doi.org/10.1016/j.memsci.2025.124231.

Data availability

Data will be made available on request.

References

[1] S. Najari, S. Saeidi, P. Concepcion, D.D. Dionysiou, S.K. Bhargava, A.F. Lee, K. Wilson, Oxidative dehydrogenation of ethane: Catalytic and mechanistic aspects and future trends, Chem. Soc. Rev. 50 (2021) 4564–4605, https://doi.org/10.1039/D0CS01518K.

[2] H. Wang, M. Fan, Z. Zhang, J. Hao, C. Wang, Control of cryogenic extractive distillation process for separating CO_2–C_2H_6 azeotrope, Comput. Chem. Eng. 128 (2019) 384–391, https://doi.org/10.1016/j.compchemeng.2019.06.017.

[3] H. Wang, C. Wang, Z. Zhang, F. Li, M. Fan, Application of feed-splitting in extractive distillation in the separation of the CO_2-C_2H_6 azeotrope for recovering light hydrocarbon, Energy Sources Part A-Recovery Util. Environ. Eff. 46 (2024) 14687–14698, https://doi.org/10.1080/15567036.2020.1808121.

[4] B. Liu, M. Zhang, T. Wang, W. Jia, Process simulation of CO_2 capture from CO_2-EOR associated petroleum gas with aqueous MEA and MDEA solvents, Energy Sci. Eng. 7 (2019) 663–675, https://doi.org/10.1002/ese3.308.

[5] Y. Li, Y. Wang, D. Li, Y. Li, C. Yao, X. Chen, W. Huang, Novel design for a green and economical CO_2 recovery process in CO_2-enhanced oil recovery, Energy Fuels 39 (2025) 2084–2097, https://doi.org/10.1021/acs.energyfuels.4c04752.

[6] E. Drioli, A.I. Stankiewicz, F. Macedonio, Membrane engineering in process intensification—An overview, J. Membr. Sci. 380 (2011) 1–8, https://doi.org/10.1016/j.memsci.2011.06.043.

[7] D.S. Sholl, R.P. Lively, Seven chemical separations to change the world, Nature 532 (2016) 435–437, https://doi.org/10.1038/532435a.

[8] L. Yu, M.S. Nobandegani, J. Hedlund, Industrially relevant CHA membranes for CO_2/CH_4 separation, J. Membr. Sci. 641 (2022) 119888, https://doi.org/10.1016/j.memsci.2021.119888.

[9] N. Kosinov, C. Auffret, C. Gücüyener, B.M. Szyja, J. Gascon, F. Kapteijn, E.J. M. Hensen, High flux high-silica SSZ-13 membrane for CO_2 separation, J. Mater. Chem. A 2 (2014) 13083–13092, https://doi.org/10.1039/C4TA02744B.

[10] K. Aoki, K. Kusakabe, S. Morooka, Separation of gases with an A-type zeolite membrane, Ind. Eng. Chem. Res. 39 (2000) 2245–2251, https://doi.org/10.1021/ie990902c.

[11] J. Caro, M. Noack, P. Kölsch, Zeolite membranes: From the laboratory scale to technical applications, Adsorption 11 (2005) 215–227, https://doi.org/10.1007/s10450-005-5394-9.

[12] N. Kosinov, J. Gascon, F. Kapteijn, E.J.M. Hensen, Recent developments in zeolite membranes for gas separation, J. Membr. Sci. 499 (2016) 65–79, https://doi.org/10.1016/j.memsci.2015.10.049.

[13] C. Algieri, E. Drioli, Zeolite membranes: Synthesis and applications, Sep. Purif. Technol. 278 (2021) 119295, https://doi.org/10.1016/j.seppur.2021.119295.

[14] B. Yue, S. Liu, Y. Chai, G. Wu, N. Guan, L. Li, Zeolites for separation: Fundamental and application, J. Energy Chem. 71 (2022) 288–303, https://doi.org/10.1016/j.jechem.2022.03.035.

[15] L.J. Smith, H. Eckert, A.K. Cheetham, Site preferences in the mixed cation zeolite, Li, Na-chabazite: A combined solid-state NMR and neutron diffraction study, J. Am. Chem. Soc. 122 (2000) 1700–1708, https://doi.org/10.1021/ja992882b.

[16] A. Taherizadeh, A. Simon, H. Richter, M. Stelter, I. Voigt, Characterization and synthesis of high permeance SSZ-13 membranes to separate CO_2 from CH_4 for biogas upgrading, J. Membr. Sci. 703 (2024) 122845, https://doi.org/10.1016/j.memsci.2024.122845.

[17] X. Mo, H. Liu, Y. Li, Q. Gu, B. Wang, R. Zhou, W. Xing, SSZ-13 membranes on novel silica carbide monoliths for efficient CO_2 separation, J. Membr. Sci. 699 (2024) 122642, https://doi.org/10.1016/j.memsci.2024.122642.

[18] X. Peng, L. Chen, L. You, Y. Jin, C. Zhang, S. Ren, F. Kapteijn, X. Wang, X. Gu, Improved synthesis of hollow fiber SSZ-13 zeolite membranes for high-pressure CO_2/CH_4 separation, Angew. Chem. Int. Ed. 63 (2024) e202405969, https://doi.org/10.1002/anie.202405969.

[19] X. Li, K. Yu, Z. He, B. Liu, R. Zhou, W. Xing, Improved SSZ-13 thin membranes fabricated by seeded-gel approach for efficient CO_2 capture, Chin. J. Chem. Eng. 56 (2023) 273–280, https://doi.org/10.1016/j.cjche.2022.07.012.

[20] Y. Jeong, M. Lee, G. Lee, S. Hong, E. Jang, N. Choi, J. Choi, Unavoidable but minimizable microdefects in a polycrystalline zeolite membrane: Its remarkable performance for wet CO_2/CH_4 separation, J. Mater. Chem. A 9 (2021) 12593–12605, https://doi.org/10.1039/D1TA01286J.

[21] H. Qiu, Y. Zhang, L. Kong, X. Kong, X. Tang, D. Meng, N. Xu, M. Wang, Y. Zhang, High performance SSZ-13 membranes prepared at low temperature, J. Membr. Sci. 603 (2020) 118023, https://doi.org/10.1016/j.memsci.2020.118023.

[22] M. Zhou, L. Yu, J. Hedlund, Ultrathin DDR films with exceptionally high CO_2 flux and uniformly adjustable orientations, Adv. Funct. Mater. 32 (2022) 2112427, https://doi.org/10.1002/adfm.202112427.

[23] D. Kim, S. Ghosh, N. Akter, A. Kraetz, X. Duan, G. Gwak, N. Rangnekar, J. R. Johnson, K. Narasimharao, M.A. Malik, S. Al-Thabaiti, B. McCool, J. A. Boscoboinik, K.A. Mkhoyan, M. Tsapatsis, Twin-free, directly synthesized MFI nanosheets with improved thickness uniformity and their use in membrane fabrication, Sci. Adv. 8 (2022) eabm8162, https://doi.org/10.1126/sciadv.abm8162.

[24] X. Duan, D. Kim, K. Narasimharao, S. Al-Thabaiti, M. Tsapatsis, High-performance ammonia-selective MFI nanosheet membranes, Chem. Commun. 57 (2021) 580–582, https://doi.org/10.1039/d0cc07217f.

[25] W. Mei, Y. Du, T. Wu, F. Gao, B. Wang, J. Duan, J. Zhou, R. Zhou, High-flux CHA zeolite membranes for H_2 separations, J. Membr. Sci. 565 (2018) 358–369, https://doi.org/10.1016/j.memsci.2018.08.025.

[26] M.L. Gualtieri, C. Anderson, F. Jareman, J. Hedlund, A.F. Gualtieri, M. Leoni, C. Meneghini, Crack formation in α-alumina supported MFI zeolite membranes studied by *in situ* high temperature synchrotron powder diffraction, J. Membr. Sci. 290 (2007) 95–104, https://doi.org/10.1016/j.memsci.2006.12.018.

[27] J.H. Dong, Y.S. Lin, M.Z.C. Hu, R.A. Peascoe, E.A. Payzant, Template-removal-associated microstructural development of porous-ceramic-supported MFI zeolite membranes, Microporous Mesoporous Mater. 34 (2000) 241–253, https://doi.org/10.1016/s1387-1811(99)00175-4.

[28] J. Zhao, T. Luo, X. Zhang, Y. Lei, K. Gong, Y. Yan, Highly selective zeolite membranes as explosive preconcentrators, Anal. Chem. 84 (2012) 6303–6307, https://doi.org/10.1021/ac301359j.

[29] S. Yang, Y.H. Kwon, D.-Y. Koh, B. Min, Y. Liu, S. Nair, Highly selective SSZ-13 zeolite hollow fiber membranes by ultraviolet activation at near-ambient temperature, ChemNanoMat 5 (2019) 61–67, https://doi.org/10.1002/cnma.201800272.

[30] G. Li, S. Fan, Z. Zhang, Y. Wang, X. Lang, J. Li, Mild ultraviolet detemplation of SAPO-34 zeolite membranes toward pore structure control and highly selective gas separation, Sep. Purif. Technol. 318 (2023) 123988, https://doi.org/10.1016/j.seppur.2023.123988.
[31] J. Zhou, S. Wu, B. Liu, R. Zhou, W. Xing, Scalable fabrication of highly selective SSZ-13 membranes on 19-channel monolithic supports for efficient CO_2 capture, Sep. Purif. Technol. 293 (2022) 121122, https://doi.org/10.1016/j.seppur.2022.121122.
[32] S. Park, M. Lee, S. Hong, Y. Jeong, D. Kim, N. Choi, J. Nam, H. Baik, J. Choi, Low-temperature ozone treatment for *p*-xylene perm-selective MFI type zeolite membranes: Unprecedented revelation of performance-negating cracks larger than 10 nm in polycrystalline membrane structures, J. Membr. Sci. 668 (2023) 121212, https://doi.org/10.1016/j.memsci.2022.121212.
[33] K. Wu, Z. Song, H. Chen, Y. Zhang, X. Gu, Synthesis of all-silica ZSM-58 zeolite membranes on hollow fibers for CO_2/H_2 separation, Int. J. Hydrogen Energy 78 (2024) 524–533, https://doi.org/10.1016/j.ijhydene.2024.06.320.
[34] L. Peng, Z. Duan, S. Cen, X. Gu, Tungsten-doped high-silica CHA zeolite membranes with improved hydrophobicity for CO_2 separation, Sep. Purif. Technol. 342 (2024) 126922, https://doi.org/10.1016/j.seppur.2024.126922.
[35] F. Ye, S. Fan, X. Lang, Y. Wang, G. Li, Organic template residues confined in silicalite-1 zeolite membranes for tuning pore structures and boosting H_2/CO_2 separation, Sep. Purif. Technol. 346 (2024) 127362, https://doi.org/10.1016/j.seppur.2024.127362.
[36] Y. Li, S. He, C. Shu, X. Li, B. Liu, R. Zhou, Z. Lai, A facile approach to synthesize SSZ-13 membranes with ultrahigh N_2 permeances for efficient N_2/CH_4 separations, J. Membr. Sci. 632 (2021) 119349, https://doi.org/10.1016/j.memsci.2021.119349.
[37] R. Xu, R. Zhang, N. Liu, B. Chen, S.Z. Qiao, Template design and economical strategy for the synthesis of SSZ-13 (CHA-type) zeolite as an excellent catalyst for the selective catalytic reduction of NO_x by ammonia, ChemCatChem 7 (2015) 3842–3847, https://doi.org/10.1002/cctc.201500771.
[38] Y. Guo, T. Sun, X. Liu, Q. Ke, X. Wei, Y. Gu, S. Wang, Cost-effective synthesis of CHA zeolites with controllable morphology and size, Chem. Eng. J. 379 (2019) 331–339, https://doi.org/10.1016/j.cej.2019.03.268.
[39] J. Tang, Y. Zhou, W. Su, X. Liu, Y. Sun, Synthesis of zeolite SSZ-13 for N_2 and CO_2 separation, Adsorpt. Sci. Technol. 31 (2013) 549–558, https://doi.org/10.1260/0263-6174.31.6.549.
[40] R. Zhou, H. Wang, B. Wang, X. Chen, S. Li, M. Yu, Defect-patching of zeolite membranes by surface modification using siloxane polymers for CO_2 separation, Ind. Eng. Chem. Res. 54 (2015) 7516–7523, https://doi.org/10.1021/acs.iecr.5b01034.
[41] Q. Zhang, H. Su, J. Luo, Y. Wei, A magnetic nanoparticle supported dual acidic ionic liquid: A “quasi-homogeneous” catalyst for the one-pot synthesis of benzoxanthenes, Green Chem. 14 (2012) 201–208, https://doi.org/10.1039/C1GC16031A.
[42] H. Wang, M. Zhu, T. Wu, Q. Jiang, F. Zhang, Y. Wu, X. Chen, Template removal and surface modification of an SSZ-13 membrane with heated sodium chloride for CO_2/CH_4 gas separation, ACS Omega 7 (2022) 6721–6727, https://doi.org/10.1021/acsomega.1c06215.
[43] A. Bordoloi, S. Sahoo, F. Lefebvre, S.B. Halligudi, Heteropoly acid-based supported ionic liquid-phase catalyst for the selective oxidation of alcohols, J. Catal. 259 (2008) 232–239, https://doi.org/10.1016/j.jcat.2008.08.010.
[44] L. Lang, S. Zhao, J. Jiang, W. Yang, X. Yin, Importance of hydrogen for low-temperature detemplation of high-silica MFI zeolite crystals, Microporous Mesoporous Mater. 235 (2016) 143–150, https://doi.org/10.1016/j.micromeso.2016.07.044.
[45] O. Pachtová, M. Kocirik, A. Zikánová, B. Bernauer, S. Miachon, J.A. Dalmon, A comparative study of template removal from silicalite-1 crystals in pyrolytic and oxidizing regimes, Microporous Mesoporous Mater. 55 (2002) 285–296, https://doi.org/10.1016/S1387-1811(02)00430-4.
[46] I. Jirka, P. Sazama, A. Zikánová, P. Hrabánek, M. Kocirik, Low-temperature thermal removal of template from high silica ZSM-5. Catalytic effect of zeolitic framework, Microporous Mesoporous Mater. 137 (2011) 8–17, https://doi.org/10.1016/j.micromeso.2010.08.015.
[47] P. Zhou, T. Wu, Z. Sun, Y. Liu, X. Chen, M. Zhu, F. Zhang, N. Hu, Y. Li, T. Gui, X. Chen, H. Kita, Influence of sodium ion on high-silica SSZ-13 membranes for efficient CO_2/CH_4 and N_2/CH_4 separations, J. Membr. Sci. 661 (2022) 120918, https://doi.org/10.1016/j.memsci.2022.120918.
[48] W. Bo, S. Ren, L. You, X. Meng, Y. Ji, X. Peng, M. Zhu, C. Zhang, X. Wang, X. Gu, Fabrication of high-quality SSZ-13 zeolite membranes for efficient SF_6 recovery, J. Membr. Sci. 690 (2024) 122200, https://doi.org/10.1016/j.memsci.2023.122200.
[49] T. Wu, Z. Huang, Z. Sun, J. Zeng, Y. Xiao, H. Wu, R. Wu, B. Liu, M. Zhu, F. Zhang, X. Chen, H. Kita, Fluoride-free synthesis of SSZ-13 zeolite membranes from clear-solution with reduced time, Sep. Purif. Technol. 361 (2025) 131235, https://doi.org/10.1016/j.seppur.2024.131235.
[50] S. Song, F. Gao, Y. Zhang, X. Li, M. Zhou, B. Wang, R. Zhou, Preparation of SSZ-13 membranes with enhanced fluxes using asymmetric alumina supports for N_2/CH_4 and CO_2/CH_4 separations, Sep. Purif. Technol. 209 (2019) 946–954, https://doi.org/10.1016/j.seppur.2018.09.016.
[51] W. Chen, F. Ye, S. Fan, Y. Wang, X. Lang, Z. Zhang, G. Li, Manipulating pore structures of SSZ-13 zeolite membranes via hydrocracking activation for superior H_2/CO_2 separation, Microporous Mesoporous Mater. 387 (2025) 113518, https://doi.org/10.1016/j.micromeso.2025.113518.
[52] J. van den Bergh, S. Ban, T.J.H. Vlugt, F. Kapteijn, Diffusion in zeolites: extension of the relevant site model to light gases and mixtures thereof in zeolites DDR, CHA, MFI and FAU, Sep. Purif. Technol. 73 (2010) 151–163, https://doi.org/10.1016/j.seppur.2010.03.018.
[53] N.O. Chisholm, H.H. Funke, R.D. Noble, J.L. Falconer, Carbon dioxide/alkane separations in a SSZ-13 membrane, J. Membr. Sci. 568 (2018) 17–21, https://doi.org/10.1016/j.memsci.2018.09.049.
[54] T. Wu, C. Shu, S. Liu, B. Xu, S. Zhong, R. Zhou, Separation performance of Si-CHA zeolite membrane for a binary H_2/CH_4 mixture and ternary and quaternary mixtures containing impurities, Energy Fuels 34 (2020) 11650–11659, https://doi.org/10.1021/acs.energyfuels.0c01720.
[55] C. Gong, X. Peng, M. Zhu, T. Zhou, L. You, S. Ren, X. Wang, X. Gu, Synthesis and performance of STT zeolite membranes for He/N_2 and He/CH_4 separation, Sep. Purif. Technol. 301 (2022) 121927, https://doi.org/10.1016/j.seppur.2022.121927.